







Evolution of magnetism in the magnetic topological semimetal $\text{NdSb}_x\text{Te}_{2-x+\delta}$

Santosh Karki Chhetri ¹, Rabindra Basnet ^{1,2,*}, Jian Wang ⁴, Krishna Pandey ³, Gokul Acharya,¹
Md Rafique Un Nabi ¹, Dinesh Upreti,¹ Josh Sakon,⁵ Mansour Mortazavi,² and Jin Hu ^{1,3,†}

¹Department of Physics, University of Arkansas, Fayetteville, Arkansas 72701, USA

²Department of Chemistry and Physics, University of Arkansas at Pine Bluff, Pine Bluff, Arkansas 71603, USA

³Materials Science and Engineering Program, Institute for Nanoscience and Engineering, University of Arkansas, Fayetteville, Arkansas 72701, USA

⁴Department of Chemistry and Biochemistry, Wichita State University, Wichita, Kansas 67260, USA

⁵Department of Chemistry and Biochemistry, University of Arkansas, Fayetteville, Arkansas 72701, USA

 (Received 12 October 2023; revised 28 March 2024; accepted 22 April 2024; published 13 May 2024)

Magnetic topological semimetals $Ln\text{SbTe}$ (Ln = lanthanide) have attracted intensive attention because of the presence of interplay between magnetism, topological, and electron correlations depending on the choices of magnetic Ln elements. Recently, varying Sb-Te composition has been found to effectively control the electronic and magnetic states in $Ln\text{Sb}_x\text{Te}_{2-x}$. With this motivation, we report the evolution of magnetic properties with Sb-Te substitution in $\text{NdSb}_x\text{Te}_{2-x+\delta}$, ($0 \leq x \leq 1$). Our work reveals the interesting nonmonotonic change in magnetic ordering temperature with varying composition stoichiometry. In addition, reducing the Sb content x drives the reorientation of moments from in-plane (ab -plane) to out-of-plane (c -axis) direction that results in the distinct magnetic structures for two end compounds NdTe_2 ($x = 0$) and NdSbTe ($x = 1$). Furthermore, the moment orientation in $\text{NdSb}_x\text{Te}_{2-x+\delta}$ is also found to be strongly tunable upon application of a weak magnetic field, leading to rich magnetic phases depending on the composition stoichiometry, temperature, and magnetic field. Such strong tuning of magnetism in this material establishes it as a promising platform for investigating tunable topological states and correlated topological physics.

DOI: [10.1103/PhysRevB.109.184429](https://doi.org/10.1103/PhysRevB.109.184429)

I. INTRODUCTION

Topological semimetals (TSMs) such as Dirac or Weyl semimetals feature symmetry-protected linearly dispersed Dirac or Weyl cones in their electronic structures, which host relativistic fermions with low-energy excitations, can be described by Dirac or Weyl equations, respectively [1,2]. In contrast to Dirac or Weyl nodes at discrete points in the momentum space in Dirac and Weyl semimetals, another class of TSMs, i.e., nodal-line semimetals, exhibit interesting linear band crossings along one-dimensional loops or lines. Various exotic properties have been discovered, such as large magnetoresistance [3], ultrahigh mobility [3], chiral anomaly [4,5], and surface Fermi arcs [6–9], providing a deeper understanding of fundamental topological physics as well as opportunities for future technological applications. Within these categories of TSMs, there has recently been rapidly growing interest in magnetic TSMs such as $\text{Co}_2\text{Mn}(\text{Al}/\text{Ga})$ [10–14], $\text{Co}_3\text{Sn}_2\text{S}_2$ [15,16], FeSn [17], Fe_3Sn_2 [18], $\text{Fe}_3(\text{Al}/\text{Ga})$ [19], Fe_3GeTe_2 [20], $\text{Mn}_3(\text{Ge}/\text{Sn})$ [21–24], and GdPtBi [25]. These compounds offer a rare platform to investigate the interplay between magnetism and nontrivial band topology, which can generate novel exotic quantum phenomena such as large intrinsic anomalous Hall effect [26] and anomalous Nernst effect [27].

As described above, the magnetism in the majority of magnetic TSMs reported so far originates from $3d$ transition metal elements. In addition to transition metal-based compounds, magnetic lanthanide (Ln)-based TSMs are also highly desired because of strong correlation effects brought about by the $4f$ electrons. The $Ln\text{SbTe}$ compounds represent one such model example [28–44]. $Ln\text{SbTe}$ belongs to the ZrSiS -type nodal-line semimetal family, which can be represented by a general chemical formula WHM ($W = \text{Zr}/\text{Hf}/\text{lanthanides}$; $H = \text{Si}/\text{Ge}/\text{Sn}/\text{Sb}$, $M = \text{S}, \text{Se}, \text{Te}$). Those materials crystallize in a layered PbFCl -type crystal structure (space group $P4/nmm$), characterized by square or nearly square net layers of H atoms that harbor relativistic fermions [28,31,45–60]. In $Ln\text{SbTe}$, the presence of a magnetic Ln element such as Ce [28–30], Nd [37,38,44], Sm [35,36], Gd [31–33], Tb [42,43], Dy [41,44], Ho [39,40,43], and Er [44] activates the spin degree of freedom that leads to diverse antiferromagnetic (AFM) ground states depending on the choice of Ln [28,31,35,37,39,41,44]. Varying the Ln element is also found to tune the topological states generated by Sb layers [28,30,31,35,39–41,57,58,61], providing an opportunity to engineer band topology via coupling between magnetism and electronic bands [28]. Furthermore, rich quantum phenomena such as the Kondo effect, charge density waves (CDWs), and correlation enhancement have been reported in various $Ln\text{SbTe}$ compounds [28,29,33–35,37,61,62], which are also strongly dependent on the choices of Ln elements.

Besides magnetism from Ln , tuning Sb-Te composition stoichiometry has been established as an effective approach

*basnetr@uapb.edu

†jinhu@uark.edu

TABLE I. Elemental compositions used in the source materials and final compositions in the grown crystals determined by EDXS.

Source materials			EDS composition	NdSb _x Te _{2-x+δ}	
Nd	Sb	Te		<i>x</i>	δ
1	0	2	NdTe ₂	0	0
1	1.2	1	NdSb _{0.10} Te _{1.93}	0.10	0.03
1	0.5	1.5	NdSb _{0.29} Te _{1.73}	0.29	0.02
1	0.2	0.8	NdSb _{0.45} Te _{1.57}	0.45	0.02
1	1.1	0.9	NdSb _{0.60} Te _{1.48}	0.60	0.08
1	0.3	0.7	NdSb _{0.82} Te _{1.22}	0.82	0.04
1	1.2	0.8	NdSb ₁ Te _{1.08}	1	0.08

to engineer electronic and magnetic phases in $LnSb_xTe_{2-x}$ [30,33,34,36,61,63]. Given that the square-net lattices are inherently unstable [64], doping electrons by substituting Te for Sb causes distortion of the Sb-square net and the subsequent formation of CDWs, which has been found to modify electronic band structures and intrinsic magnetism [30,33,34,36,61,63]. In $LnSb_xTe_{2-x}$, the magnetism has been found to be effectively tunable with varying Sb composition x ; however, the Sb-Te substitution induces distinct evolution of magnetic properties in few $LnSbTe$ ($Ln = Ce$ [30], Sm [36], and Gd [33,34]) compounds despite the similar crystal symmetry and structure evolution from tetragonal (space group $P4/nmm$) to orthorhombic (space group $Pmmm$) phase in off-stoichiometric compositions. While numerous stoichiometric $LnSbTe$ compounds [28,29,33–35,37,61,62] have been discovered, the evolution of magnetism by tuning composition in off-stoichiometric compounds is still in an early stage. Only recently, a neutron diffraction study has determined the modification of magnetic structure with varying Sb-Te composition in NdSb_{0.94}Te_{0.92} and NdSb_{0.48}Te_{1.37} [63]. Such promising results demand a complete understanding of magnetism and possible tuning of topological states over the entire Sb-Te composition in NdSb_xTe_{2-x}. In this work, we present the evolution of magnetic properties from $x = 0$ to 1 in NdSb_xTe_{2-x}. Our work reveals an interesting nonmonotonic variation of magnetic ordering temperature (T_N) and the reorientation of Nd moments with Sb-Te substitution. These results provide a rich platform for tunable topological states and further studying the correlated topological physics.

II. EXPERIMENT

The NdSb_xTe_{2-x+δ} ($0 \leq x \leq 1$, δ represents possible vacancies) single crystals used in this work were synthesized by a chemical vapor transport (CVT) method using I₂ as the transport agent. The pristine NdTe₂ was grown by a direct CVT method with elementary Nd and Te powders as source materials. For each of the other compositions with Sb, a polycrystalline precursor is necessary to minimize vacancies (as discussed below). Each precursor was prepared by heating the mixture of Nd with different ratios of Sb and Te powders (shown in Table I) at 850 °C for 2 days. The single crystals were obtained via CVT with a temperature gradient from 1000 to 850 °C for 2 weeks. The elemental compositions and crystal structures of the obtained crystals were examined by energy-

dispersive x-ray spectroscopy (EDXS) and x-ray diffraction (XRD), respectively. Magnetization measurements up to 9 T were performed by using a physical property measurement system (Quantum Design). Magnetization measurements up to 7 T and angular-dependent magnetization were performed by using a magnetic property measurement system (MPMS, Quantum Design) equipped with a rotator.

III. RESULT AND DISCUSSION

A recent surge of interest in TSMs featuring a square net of atoms has motivated the study of the $LnSbTe$ family [28–44]. While the square-net planes in the majority of WHM compounds are formed by group-IV elements $H = Si, Ge, \text{ and } Sn$ [45–56,65], a Sb (group-V) square net sandwiched by Ln -Te bilayers is present in $LnSbTe$ compounds. Previous studies have demonstrated that the synthesis of ideal stoichiometric $LnSbTe$ compounds is challenging [29,37,63] and often yields various off-stoichiometric $LnSb_xTe_{2-x}$ ($0 < x < 1$) compositions consisting of a distorted Sb plane [30,33,34,36,61,63]. Such off-stoichiometry is also accompanied by vacancies in the Sb [33,34,36,62,63] and Te [30,33,61,63] layers that enhance with reducing Sb content [34,36,63], and eventually, after complete substitution of Te for Sb, produces a strong Te vacancy in structurally similar $LnTe_2$ compounds [66,67]. The chalcogen vacancy widely occurs in LnX_2 ($X = S, Se, \text{ and } Te$), which has been ascribed to the presence of mixed anions $(X_2)^{2-}$ and $(X)^{2-}$ in the chalcogen layer [67,68] and favored by decreasing the Ln^{3+} cation radius along the lanthanide series [68]. Therefore, chalcogen vacancy is usually seen in compounds with smaller Ln^{3+} cations such as NdTe_{1.89} [66], SmTe_{1.84} [69], GdTe_{1.80} [70], TbTe_{1.80} [70], and DyTe_{1.80} [70]. Replacing Sb for Te in these compounds induces hole doping and consequently reduces the number of vacancies required for charge balance in Te layers [34].

In NdSb_xTe_{2-x} studied in this work, both slight [63] and the lack [44] of Te vacancy are observed in a nearly stoichiometric composition. Although an earlier study on CeSb_xTe_{2-x-δ} [30] has claimed less effect of Te vacancy on magnetization, we selected NdSb_xTe_{2-x} samples with minimum vacancy to ensure the systematic tuning of magnetization with varying composition and without the interference of vacancy effects. The millimeter-size single crystals in the whole compositional range from NdTe₂ ($x = 0$) to NdSbTe_{1.08} ($x = 1$) were obtained using CVT [Fig. 1(a)], similar to previous NdSbTe growths [37,38,44]. Our EDXS results have revealed the nearly 1:2 stoichiometric composition ratio between Nd and (Sb+Te) (Table I), from which we conclude the absence of vacancies within the resolution limit of our instrument. Such observation is in contrast to the reported Ce, Sm, and Gd sibling compounds [30,33,34,36,62], which might be due to the slight difference in synthesis method and sample screening. However, we observed a slight excess of Te in our composition analysis. Therefore, our samples can be represented as NdSb_xTe_{2-x+δ}, where $\delta = 0-0.08$ denotes the excess Te that might be due to the instrument error or partial accommodation into the Sb layer, as seen in CeSbTe [29] and GdSbTe [34]. As shown in Table I, the nominal composition in source materials is found to yield significantly

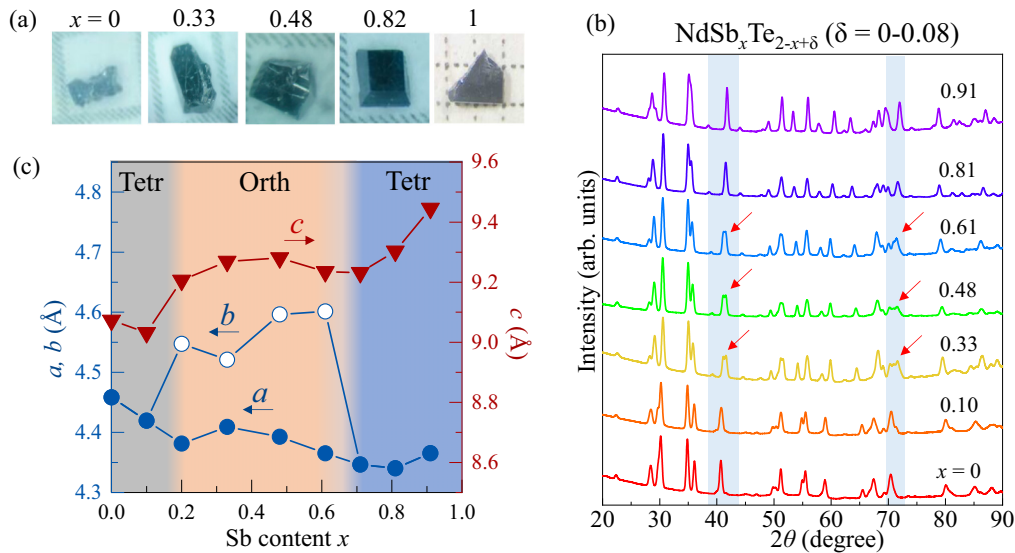


FIG. 1. (a) Optical microscope images of $\text{NdSb}_x\text{Te}_{2-x+\delta}$ ($0 \leq x \leq 1$) crystals. (b) X-ray diffraction result for $\text{NdSb}_x\text{Te}_{2-x+\delta}$. (c) Evolution of lattice parameters a , b (left vertical axis), and c (right vertical axis) with varying Sb content x . The blue, orange, and gray regions represent tetragonal (Tetr), orthorhombic (Orth), and tetragonal (Tetr) lattices, respectively.

different composition (determined by EDXS) in the grown crystals, consistent with previous Sb-Te substitution studies in this family [34,36]. Earlier work on $\text{GdSb}_x\text{Te}_{2-x-\delta}$ has adopted a strategy of adding more Sb in the starting materials to obtain crystals with increasing x [34]. In contrast, we did not observe a systematic correlation between nominal and final compositions among the grown crystals (Table I), indicating the difficulty to control composition stoichiometry in $\text{NdSb}_x\text{Te}_{2-x+\delta}$. This could be the reason for the lack of a complete Sb-Te evolution study for this compound although NdSbTe [37] was one of the earliest studied LnSbTe compounds.

The stoichiometric LnSbTe compounds crystallize in tetragonal (space group $P4/nmm$) structure [28–44], which on substituting Te for Sb results in structure transition to orthorhombic phase at around $x = 0.7$ to 0.85 in $\text{LnSb}_x\text{Te}_{2-x}$ ($\text{Ln} = \text{Ce}$ [30], Sm [36], and Gd [34]). The structural information determined by our structure refinement using powder XRD spectra presented in Fig. 1(b) also reveals an orthorhombic distortion at around $x \approx 0.70$ in $\text{NdSb}_x\text{Te}_{2-x+\delta}$ that is accompanied by a shrinking c axis and an expanding ab plane [Fig. 1(c)], consistent with other $\text{LnSb}_x\text{Te}_{2-x}$ ($\text{Ln} = \text{Ce}$, Sm , and Gd) members [30,34,36]. The tetragonal crystal lattice is retained on further decreasing the Sb content below $x \approx 0.18$ leading to the tetragonal structure for NdTe_2 ($x = 0$). Both tetragonal and orthorhombic structures have been reported in Te-deficient compounds $\text{NdTe}_{1.80}$ [71] and $\text{NdTe}_{1.89}$ [66], respectively. The tetragonal structure has been identified in analogous compounds CeTe_2 [72] and PrTe_2 [73] whereas LaTe_2 crystallizes in monoclinic structure [74]. The tetragonal and orthorhombic structures are very similar and could be difficult to distinguish during crystal structure refinement. In addition, because of the presence of CDW in this material family (especially in the Sb-less compositions), the refinement results could be influenced by the additional CDW satellite peaks. Unfortunately, the impact of CDW in the crystal struc-

ture refinement for our $\text{NdSb}_x\text{Te}_{2-x+\delta}$ samples is difficult to clarify due to instrument limitation of our x-ray diffractometer. For this, a synchrotron light source is needed, which could be the scope for future studies that might also clarify the evolution of CDWs with composition stoichiometry in $\text{NdSb}_x\text{Te}_{2-x+\delta}$. Though we are not able to examine CDWs due to instrumental limitations, the reemergence of tetragonal structure for $x < 0.18$ in $\text{NdSb}_x\text{Te}_{2-x+\delta}$ can be understood by the evolution of XRD spectra with varying composition stoichiometry. As shown in Fig. 1(b), the XRD spectra display clear peak splitting for samples with intermediate Sb content (indicated by the red arrows), which is consistent with the lowering symmetry from tetragonal to orthorhombic.

With the orthorhombically distorted lattice, the two-dimensional Sb-square net characterized by identical Sb-Sb bonding length and 90° bonding angles in stoichiometry has been found to undergo deviation of bonding angles from 90° with reducing Sb content, which indicates the distorted Sb-square plane [30,34,36,63]. Distorted Sb-square nets in orthorhombic crystal lattice depending on the composition stoichiometry in LnSbTe are reported to drive tunable CDWs [30,33,34,36,61,63]. Even the formation of CDWs has been revealed in tetragonal CeTe_2 [75–77] and PrTe_2 [75] as well as monoclinic LaTe_2 [78]. The CDW is found to strongly interplay with magnetism in LnSbTe leading to complex magnetic phases in off-stoichiometric compositions [30,33,63] and even a modification of a collinear AFM structure in a nearly stoichiometric composition to a more complex elliptical cycloid magnetic structure for a Sb-less composition in $\text{NdSb}_x\text{Te}_{2-x-\delta}$ [63]. To investigate the evolution of magnetic properties over the entire composition range in $\text{NdSb}_x\text{Te}_{2-x+\delta}$, we have measured the temperature dependence of susceptibility $\chi(T)$ under in-plane ($H \parallel ab$) and out-of-plane ($H \parallel c$) magnetic fields of $\mu_0 H = 0.1$ T [Fig. 2(a)] in order to investigate the variation of T_N and moment orientation with Sb-Te substitution. Similar to the previous studies

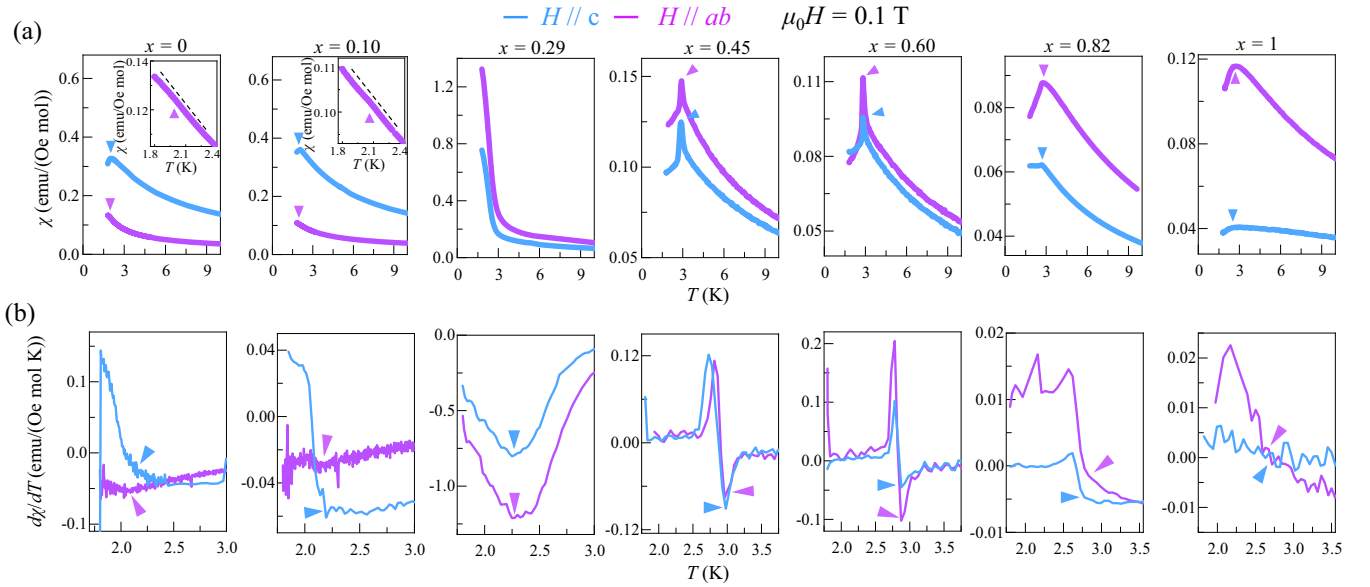


FIG. 2. (a) Temperature dependence of susceptibility for $\text{NdSb}_x\text{Te}_{2-x+\delta}$ samples under in-plane ($H\parallel ab$, magenta) and out-of-plane ($H\parallel c$, blue) magnetic fields of $\mu_0H = 0.1$ T. Inset: low-temperature susceptibility under in-plane $H\parallel ab$ field to show magnetic transition clearly. The dashed lines are a guide to the eye. (b) Temperature dependence of derivative $d\chi/dT$ of $\text{NdSb}_x\text{Te}_{2-x+\delta}$ samples. The solid triangles denote T_N .

[34,35,37,41,44], T_N for each sample, except for $x = 0.29$, is extracted from the susceptibility peak or anomaly in in-plane (χ_{\parallel} ; measured with field parallel to the ab plane) and out-of-plane (χ_{\perp} ; measured with field parallel to the c axis) susceptibility measurements, as indicated by the solid triangles in Fig. 2(a). The obtained transition temperatures are consistent with that determined from the derivative susceptibility $d\chi/dT$ [Fig. 2(b)]. Furthermore, for the $x = 0.29$ sample, which does not display clear features in susceptibility measurement, the derivative susceptibility reveals the possible magnetic transition temperature, as shown in Fig. 2(b). The extracted T_N of 2.04 K for the end compound NdTe_2 ($x = 0$) is distinct from the lack of magnetic ordering down to 2 K in $\text{NdTe}_{1.89}$ with significant Te vacancy [66]. Such difference might be attributed to the suppression of Te-mediated magnetic interaction between Nd moments. For the other end compound $\text{NdSbTe}_{1.08}$ ($x = 1$), $T_N \approx 2.74$ K is consistent with the nearly stoichiometric composition $\text{NdSb}_{0.94}\text{Te}_{0.92}$ [63] but slightly lower than the ideal stoichiometry NdSbTe ($T_N \approx 3.1$ K) [44]. In Fig. 3(a) we summarized the magnetic transition temperatures for our samples, which exhibit a nonmonotonic composition dependence. Both monotonic [30] and nonmonotonic [34] composition-dependent T_N have been observed in $\text{LnSb}_x\text{Te}_{2-x}$. In $\text{CeSb}_x\text{Te}_{2-x}$ [30], the T_N systematically increases with decreasing Sb content x , while a similar nonmonotonic composition dependence of T_N is seen in $\text{GdSb}_x\text{Te}_{2-x}$ [34]. The monotonic variation of T_N in $\text{CeSb}_x\text{Te}_{2-x}$, which is in contrast to Nd and Gd samples, might be attributed to the difference in interplay between CDWs and magnetism [63] arising from the distinct moment orientation in CeSbTe [30] as compared to NdSbTe [63] and GdSbTe [33]. In $\text{LnSb}_x\text{Te}_{2-x}$, the CDWs exhibit single modulation wave vector q within the Sb plane in the intermediate Sb-composition range i.e., $(0.21-0.34) < x <$

$(0.74-0.85)$ whereas below $x < (0.21-0.34)$ these compounds host multiple q vectors along different crystallographic axes [30,34]. The out-of-plane moment orientation in $\text{CeSb}_x\text{Te}_{2-x}$ [30] does not align with the CDW q vector, especially in the single q -vector (aligned along the ab plane) region for intermediate Sb composition, resulting in a relatively weaker interplay between CDW and magnetism, thus causing the systematic variation of T_N . On the other hand, the in-plane orientation of moments in NdSbTe [63] and GdSbTe [33] might strongly couple with the in-plane CDW q vector leading to nonmonotonic dependence of T_N with Sb-Te substitution.

As seen in Fig. 3(a), the nonmonotonic composition dependence of T_N in $\text{NdSb}_x\text{Te}_{2-x+\delta}$ involves three distinct regions featuring different orientations for Nd moments: (1) within the ab plane (represented as AFM_{ab}) for Sb-rich compositions, (2) canted configuration (cAFM) for intermediate Sb compositions, and (3) along the c axis (AFM_c) for Sb-less compositions. These moment orientations were determined by $\chi(T)$ and were further confirmed by field dependence of magnetization, $M(H)$, measurements shown in Fig. 4. Starting with pristine $\text{NdSbTe}_{1.08}$ ($x = 1$), the χ_{\parallel} gradually decreases below $T_N \approx 2.74$ K, in contrast to weakly temperature-dependent χ_{\perp} . This is suggestive of an in-plane AFM configuration, consistent with the reported magnetic structure for nearly stoichiometric $\text{NdSb}_{0.94}\text{Te}_{0.92}$ [63]. Decreasing the Sb content to $x = 0.82$, a similar $\chi(T)$ trend with unchanged T_N (≈ 2.78 K) is observed [Fig. 3(a)], indicating a similar magnetic ordering to that of the $x = 1$ compound. The in-plane easy axis is also supported by the $M(H)$ measurements under in-plane ($H\parallel ab$) and out-of-plane ($H\parallel c$) magnetic fields at $T = 2$ K. As shown in Fig. 4, for both $x = 1$ and 0.82, the in-plane (M_{\parallel} ; magnetization parallel to the ab plane) isothermal magnetization is larger than the out-of-plane (M_{\perp} ; magnetization parallel to the c axis) magnetization,

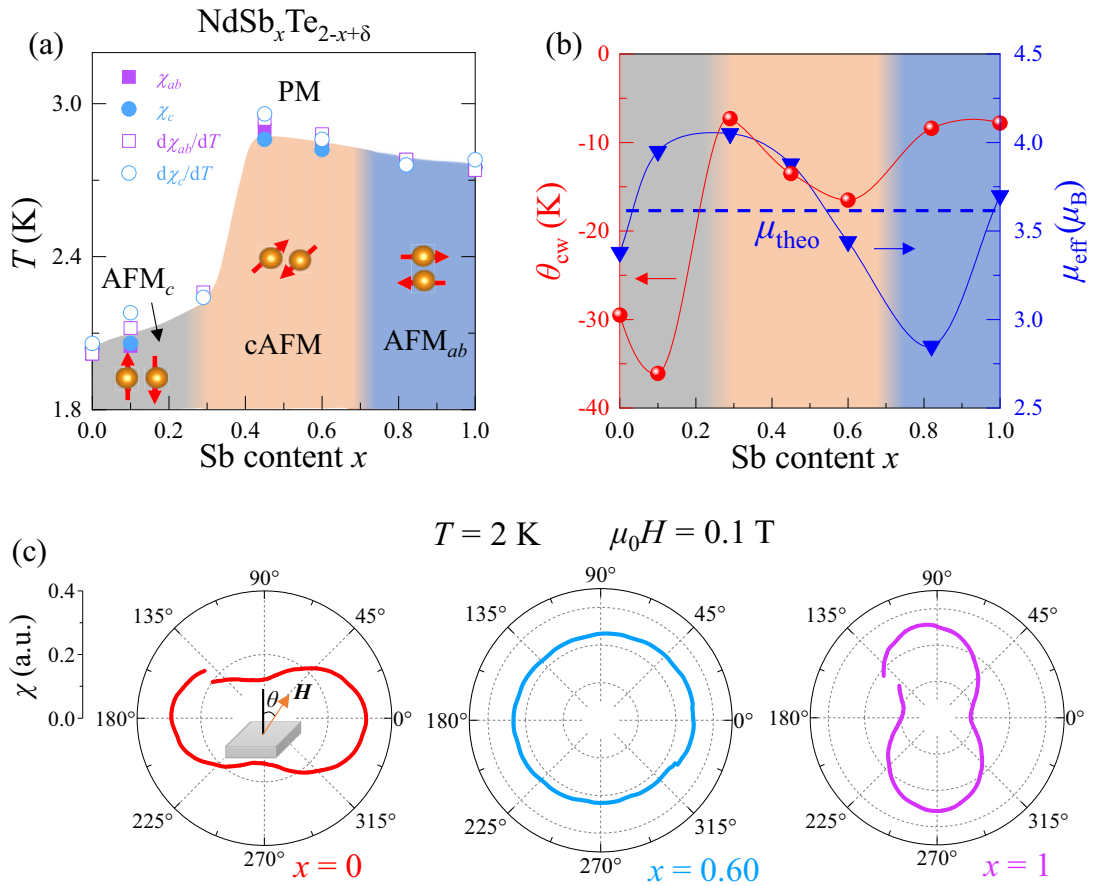


FIG. 3. (a) Evolution of T_N with varying Sb content x . Different colored regions denote distinct orientations for Nd moments. The in-plane, canted, and out-of-plane antiferromagnetic configurations are denoted as AFM_{ab} , cAFM , and AFM_c whereas PM represents a paramagnetic state. The moment orientations in each phase region are schematic to show the magnetic easy axis. Here, χ_{ab} and χ_c represent the susceptibility along the ab plane and the c axis, respectively. (b) Evolution of effective magnetic moment μ_{eff} and Curie-Weiss temperature θ_{CW} with varying Sb content x . The dashed line represents the theoretical μ_{theo} . (c) Angular dependence of susceptibility for the $x = 0, 0.60$, and 1 samples under magnetic fields of $\mu_0H = 0.1\text{ T}$ and $T = 2\text{ K}$.

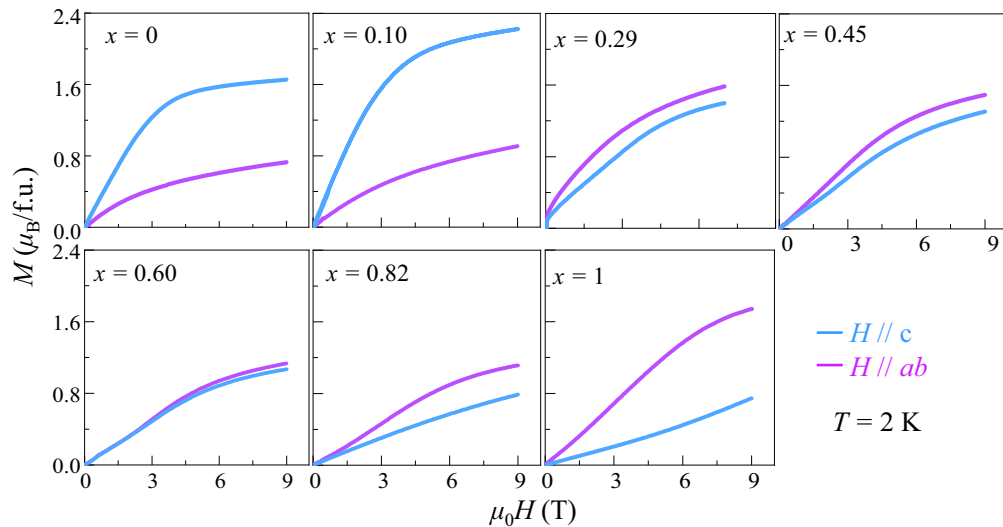


FIG. 4. Field dependence of magnetization for $\text{NdSb}_x\text{Te}_{2-x+\delta}$ samples under in-plane ($H \parallel ab$, magenta) and out-of-plane ($H \parallel c$, blue) magnetic fields at $T = 2\text{ K}$.

which implies that the easy axis should align towards the ab plane. The magnetic anisotropy in these samples is further manifested in the angular dependence of susceptibility [$\chi(\theta)$] measurements for samples representing three different AFM regions [AFM_{*ab*}, cAFM, and AFM_{*c*} in Fig. 3(a)] at $T = 2$ K and $\mu_0 H = 0.1$ T [Fig. 3(c)]. For $x = 1$, the susceptibility is maximum and minimum along the in-plane and out-of-plane fields, respectively, which is in line with the $\chi(T)$ and $M(H)$ measurements.

This scenario completely changes after entering into the orthorhombically distorted regime ($x < 0.70$). As shown in Fig. 2(a), in contrast to the Sb-rich samples that display a strong drop in χ_{\parallel} while roughly constant in χ_{\perp} , both χ_{\parallel} and χ_{\perp} exhibit clear peaks in the $x = 0.60$ sample followed by a sharp drop and then remain relatively flat down to the lowest measured temperature. Such similar temperature-dependent behavior down to the lowest measured temperature along both field directions suggests a spiral spin texture with a canted spin component [33]. The moment canting scenario is consistent with the reported elliptical cycloid magnetic structure propagating along the b axis but also with a nonzero out-of-plane component determined by neutron diffraction experiment for NdSb_{0.48}Te_{1.48} [63]. The elliptical cycloid magnetic structure with both in-plane and out-of-plane moment components can also be understood by relatively less anisotropy between field-dependent M_{\parallel} and M_{\perp} [79] at $T = 2$ K for $x = 0.60$ and 0.45 (Fig. 4). Furthermore, the weaker magnetic anisotropy in orthorhombic regime as compared to $x > 0.70$ tetragonal samples is clearly demonstrated by the lack of significant anisotropy in the $\chi(\theta)$ measurement in $x = 0.60$ [Fig. 3(c)]. Despite the well-defined peaks in both χ_{\parallel} and χ_{\perp} for $x = 0.60$, the drop of χ_{\parallel} below T_N is more pronounced than χ_{\perp} , which implies the nearly in-plane orientation for canted moments that agrees well with the higher (about three times) in-plane rather than the out-of-plane component in the elliptical cycloid magnetic structure for NdSb_{0.48}Te_{1.48} [63]. The moments remain canted for $x = 0.45$, as demonstrated by the similar magnetic transitions in both χ_{\parallel} and χ_{\perp} at a slightly higher T_N (≈ 2.9 K) but reducing the Sb content from $x = 0.60$ to 0.45 pushes the moments away from the ab plane because the decrease in χ_{\parallel} and χ_{\perp} below T_N is much more comparable than that of $x = 0.60$. The spin reorientation in the intermediate Sb regime has been attributed to the interplay between CDWs and magnetism [63], which is in line with the fact that both T_N and moment orientation essentially remain unchanged in the tetragonal regime ($x > 0.70$) where the CDW is absent [30,34]. Such coupling between CDWs and magnetism has also been proposed to relieve the magnetic frustration arising due to the competition between nearest-neighbor AFM and ferromagnetic (FM) interactions in a nearly stoichiometric NdSb_{0.94}Te_{0.92} [63]. In fact, in our $x = 1$ sample, the paramagnetic (PM) to AFM transition lacks a sharp peak but is reflected by the broad transition in χ_{\parallel} , indicating frustrated magnetic ordering consistent with a similar composition NdSb_{0.94}Te_{0.92} [63]. The broad T_N peak in $x = 1$ starts to become sharper with decreasing x leading to sharp magnetic transitions in $x = 0.60$ and 0.45 , suggesting the suppression of frustration when the CDW is functional. Furthermore, relieving the magnetic frustration would strengthen the magnetic interactions, which explains the systematic rise

of T_N with reducing the Sb content from $x = 1$ until reaching a maximum value for $x = 0.45$ [Fig. 3(a)]. The maximal T_N around $x = 0.45$ is also seen in GdSb_{*x*}Te_{2-*x*- δ} [34], suggesting a similar scenario of coupling between CDWs and in-plane magnetic moments in GdSbTe [33].

The T_N reduces on further decreasing the Sb content from $x = 0.45$ to 0.29 . The drop of T_N for $x = 0.29$ nearly coincides with the phase boundary between single and multiple CDW \mathbf{q} vectors identified in CeSb_{*x*}Te_{2-*x*- δ} [30] and GdSb_{*x*}Te_{2-*x*- δ} [34], therefore further decreasing the Sb content modifies the CDW, which is expected to tune the magnetic ordering [63]. In fact, entering into the multiple CDW \mathbf{q} -vectors regime on reduction of Sb content below $x < 0.29$, a clear magnetic transition featuring a drop in χ_{\perp} below $T_N \approx 2.01$ K for $x = 0.10$ and $T_N \approx 2.04$ K for $x = 0$ (NdTe₂) is observed. For χ_{\parallel} , the magnetic transitions in both samples manifest into weak features as shown in the insets in Fig. 2. This susceptibility behavior is distinct from the stronger susceptibility drop observed below T_N in χ_{\parallel} for Sb-rich compositions and in both χ_{\parallel} and χ_{\perp} for intermediate Sb compositions. Such susceptibility behavior showing a drop in χ_{\perp} but a weak transition in χ_{\parallel} below T_N is suggestive of the moment reorientation towards the out-of-plane direction or c axis, consistent with a much larger M_{\perp} than M_{\parallel} in $M(H)$ measurements for $x = 0.10$ and 0 (Fig. 4). In fact, the switching of magnetic anisotropy from the in-plane direction in high-Sb compositions $x = 1$ and 0.82 to the out-of-plane direction in Sb-less samples $x = 0.10$ and 0 can be directly observed in the $\chi(\theta)$ measurement. As shown in Fig. 3(c), the $\chi(\theta)$ for $x = 0$ exhibits a completely opposite trend in comparison to the $x = 1$ sample with maximum and minimum values along the out-of-plane and in-plane fields, respectively.

These results clearly demonstrate the complex interaction between CDWs and magnetism proposed in earlier Ln SbTe studies [30,33,63], which can also be understood by the evolution of magnetic parameters such as Curie-Weiss temperature (θ_{CW}) and effective magnetic moment (μ_{eff}) [Fig. 3(b)]. These parameters are extracted by fitting the $\chi(T)$ data in the paramagnetic phase using a modified Curie-Weiss model $\chi_{\text{mol}} = \chi_0 + C/(T - \theta_{CW})$, where χ_0 is the temperature-independent part of susceptibility and C is the Curie constant. From the fitting, we found negative θ_{CW} for all the samples as expected for their AFM ground state. As shown in Fig. 3(b), the θ_{CW} lacks the systematic dependence on Sb content x with significantly different θ_{CW} for two end compounds $x = 0$ ($\theta_{CW} \approx -29.5$ K) and 1 ($\theta_{CW} \approx -7.8$ K), which is distinct from the systematic variation in CeSb_{*x*}Te_{2-*x*- δ} [30] and GdSb_{*x*}Te_{2-*x*- δ} [34]. Higher (more negative) θ_{CW} for the $x = 0$ sample in comparison to the $x = 1$ sample implies a stronger AFM interaction in NdTe₂ ($x = 0$); however, its T_N is lower than that of NdSbTe_{1.08} ($x = 1$). Between these two end compounds, the variation of θ_{CW} that gives the information about magnetic exchange interactions is also unable to explain the evolution of T_N with Sb-Te substitution. Such discrepancy between the composition dependence of θ_{CW} and T_N suggests the additional contribution affecting the formation of long-range antiferromagnetic ordering in NdSb_{*x*}Te_{2-*x*+ δ} , which has also been proposed in GdSb_{*x*}Te_{2-*x*- δ} [34]. Thus, the role of CDW in tuning magnetism seems plausible in this family.

In addition, from the Curie constant we have obtained the effective moments by $\mu_{\text{eff}} = \sqrt{\frac{3k_B C}{N_A}}$, where N_A is the Avogadro's number and k_B is the Boltzmann constant. The obtained μ_{eff} also exhibits a nonmonotonic dependence on Sb content x with a value of $3.70 \mu_B$ for $\text{NdSbTe}_{1.08}$ ($x = 1$) that is slightly different than the theoretically expected value of $3.62 \mu_B$ [shown by a dashed line in Fig. 3(b)] for a Nd^{3+} ion with a $4f^3$ configuration. The μ_{eff} is further deviated from the theoretical value with increasing substitution and becomes minimum for $x = 0.82$ ($\mu_{\text{eff}} \approx 2.85 \mu_B$, which is consistent with the tetragonal to orthorhombic phase boundary that activates the CDW. On reducing the Sb content to $x = 0.60$, the μ_{eff} starts to approach the theoretical value, which is slightly surpassed on further decreasing the Sb content to $x = 0.45$ and reaching a maximum $\mu_{\text{eff}} \approx 4.05 \mu_B$ for $x = 0.29$ that appears to align with the single to multiple CDW \mathbf{q} -vectors transition below which μ_{eff} decreases to a value of $\mu_{\text{eff}} \approx 3.38 \mu_B$ for $x = 0$. Such variation of μ_{eff} also indicates the interplay between CDWs and magnetism, which is in stark contrast to $\text{CeSb}_x\text{Te}_{2-x-\delta}$ [30] and $\text{GdSb}_x\text{Te}_{2-x-\delta}$ [34] where μ_{eff} has been reported to be close to the theoretical values for the Ce^{3+} and Gd^{3+} ions, respectively, over the entire Sb-Te composition. The deviation from theoretical μ_{eff} with Sb-Te substitution in $\text{NdSb}_x\text{Te}_{2-x+\delta}$ might be attributed to a few reasons such as varying spin-orbit coupling (SOC) [80], crystal electric field (CEF) effect [81], and/or the hybridization between the $4f$ moments and conduction electrons [82–85]. The SOC is less likely to play a significant role given the fact that the Sb-Te substitution in $\text{CeSb}_x\text{Te}_{2-x-\delta}$ [30] and $\text{GdSb}_x\text{Te}_{2-x-\delta}$ [34], which would cause a similar variation of SOC, has less effect on μ_{eff} . In addition, the CEF on $4f$ electrons is negligible because they are well screened by the electrons of $5s$ and $5p$ orbitals [86,87]. This implies that the coupling of $4f$ moments and conduction electrons generated by Sb bands could cause the variation of μ_{eff} from the theoretical value. This further supports the interplay between magnetism and CDWs induced by the distorted Sb-square net. Such coupling of magnetism and CDWs might also be the origin for the reorientation of Nd moments that leads to the change in magnetic structure with Sb-Te substitution in $\text{NdSb}_x\text{Te}_{2-x+\delta}$, which is again distinct from the similar AFM configuration over an entire composition range in $\text{CeSb}_x\text{Te}_{2-x-\delta}$ [30] and $\text{GdSb}_x\text{Te}_{2-x-\delta}$ [33]. Further neutron-scattering experiments on a wide range of $\text{NdSb}_x\text{Te}_{2-x+\delta}$ compositions similar to a recent study on two Nd-based samples $\text{NdSb}_{0.94}\text{Te}_{0.92}$ and $\text{NdSb}_{0.48}\text{Te}_{1.37}$ [63] is needed to clarify the interplay between magnetism and CDWs as well as the evolution of the magnetic structure in $\text{NdSb}_x\text{Te}_{2-x+\delta}$.

The reorientation of magnetic moments has been proposed to break various symmetries and consequently tune the topological states in AFM TSMs [88–90]. For example, in a TSM candidate YbMnSb_2 [88], a C -type AFM ordering with out-of-plane or canted moments has been predicted to give rise to a gapped Dirac crossing or Weyl nodes, respectively. Similar modulation of topological states depending on moment orientation has also been predicted [89,90] and experimentally verified [89] in another TSM candidate, FeSn . Substituting Co for Fe in FeSn reorients AFM moments from

the in-plane to the out-of-plane direction, which breaks the nonsymmorphic symmetry leading to a theoretically predicted gap at the Dirac point [89]. In LnSbTe , the topological band structure can be controlled by Sb-Te substitution, providing access to an ideal Dirac state located near the Fermi level (E_F) for intermediate Sb compositions $\text{CeSb}_{0.51}\text{Te}_{1.40}$ [30] and $\text{GdSb}_{0.46}\text{Te}_{1.48}$ [61] where all trivial bands at the E_F are gapped out by CDWs. However, as discussed earlier, both $\text{CeSb}_x\text{Te}_{2-x-\delta}$ [30] and $\text{GdSb}_x\text{Te}_{2-x-\delta}$ [33] exhibit similar spin orientation for the entire Sb composition. Therefore, $\text{NdSb}_x\text{Te}_{2-x+\delta}$ studied in this work, which displays switching of the easy axis between in-plane and out-of-plane directions, could be an ideal platform to investigate the interplay between moment reorientation and nontrivial band topology.

In addition to symmetry breaking induced by moment reorientation, tuning magnetic states by applying a magnetic field has also been proposed to modify the topological phases in CeSbTe [28]. The AFM ground state in CeSbTe is found to exhibit field-driven metamagnetic transition and a subsequent FM-like polarization [28], which provides an approach to switch on/off the time-reversal symmetry and is predicted to tune topological states [28]. Also, a field-driven moment polarization to a FM state has been demonstrated to lead to a topological phase transition from an AFM topological insulator to a time-reversal symmetry-breaking Weyl state in MnBi_2Te_4 [91]. Here, as seen in the field dependence of magnetization, $M(H)$, measurements at $T = 2$ K for all $\text{NdSb}_x\text{Te}_{2-x+\delta}$ samples (Fig. 4), the isothermal magnetization becomes sublinear at high field but lacks a clear saturation behavior seen in true ferromagnets and their values at $\mu_0 H = 9$ T are smaller than the saturation moment of $3.62 \mu_B$ for a Nd^{3+} ion. Therefore, the high-field sublinear magnetization in $\text{NdSb}_x\text{Te}_{2-x+\delta}$ might be attributed to a possible new canted AFM state with partial polarization of moments. We calculated the derivative of $M(H)$ data [$dM/d(\mu_0 H)$] to precisely determine the field-driven metamagnetic (MM) transition and partial spin polarization (PP), which were used in an earlier NdSbTe study where a sharp peak followed by a broad hump or shoulder at a higher field are defined as metamagnetic transition (H_{MM}) and partial spin polarization (H_{PP}) fields, respectively [63]. The field dependence of $dM/d(\mu_0 H)$ data under $H \parallel ab$ and $H \parallel c$ fields for samples representing three different AFM regions [AFM_{ab}, cAFM, and AFM_c in Fig. 3(a)] showing H_{MM} and H_{PP} are presented in Fig. 5(a). Based on these results, we constructed a magnetic phase diagram at $T = 2$ K [Fig. 5(b)], which depicts the evolution of magnetic states with Sb content x . First, in the AFM_{ab} region, the $x = 1$ sample exhibits AFM to partial moment polarization featuring sublinear magnetization at a higher in-plane magnetic field ($H \parallel ab$) while the $x = 0.82$ sample undergoes an AFM to MM transition before partial polarization at $H \parallel ab$ only, consistent with their in-plane moments as discussed earlier. Decreasing Sb content below $x < 0.82$ systematically reduces both H_{MM} and H_{PP} in the cAFM region; however, these transitions occur under both in-plane and out-of-plane fields, which is in line with their canted moments. As mentioned above, further reducing the Sb content to $x = 0.10$ and 0 switches the easy axis towards the out-of-plane direction and thus features a transi-

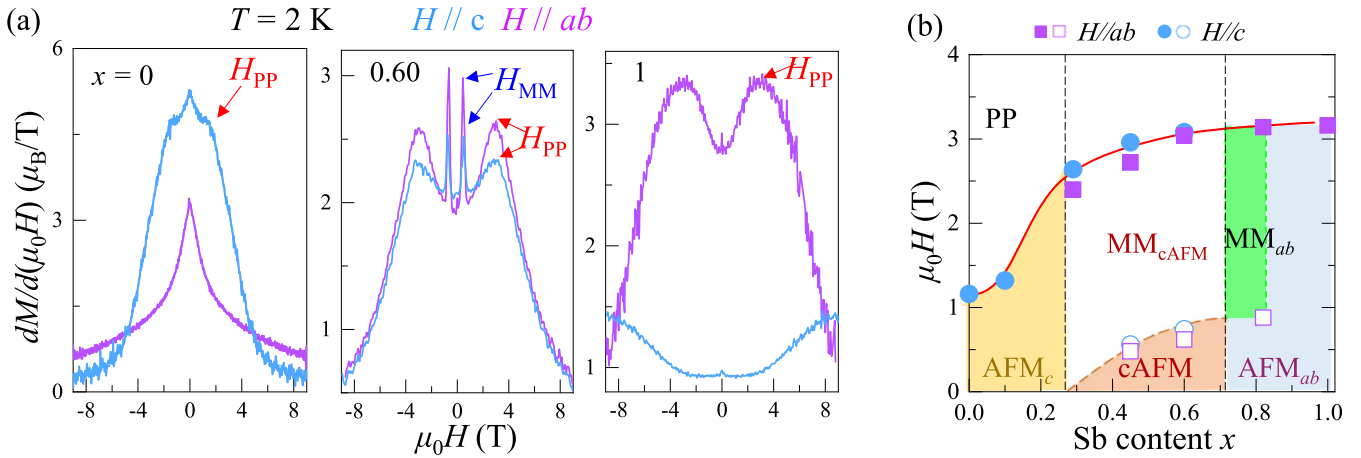


FIG. 5. (a) Field dependence of derivative $dM/d(\mu_0H)$ under in-plane ($H||ab$, magenta) and out-of-plane ($H||c$, blue) magnetic fields at $T = 2$ K. The metamagnetic and partial spin polarization fields are represented as H_{MM} (blue) and H_{PP} (red), respectively. (b) Magnetic phase diagram constructed from the field dependence of magnetization measurements presented in Fig. 3. The in-plane, canted, and out-of-plane antiferromagnetic configurations are denoted as AFM_{ab} , $cAFM$, and AFM_c . The metamagnetic transition for in-plane and canted antiferromagnetic states are represented as MM_{ab} and MM_{cAFM} , respectively. The partial spin polarization is denoted as PP.

tion from AFM to partial spin polarization (without a low-field metamagnetic transition) for the $H||c$ field only. This demonstrates rich magnetic phases in $NdSb_xTe_{2-x+\delta}$ depending on both Sb composition and applied field, which provides a rare platform to explore coupling between magnetism and electronic band topology.

In conclusion, we have investigated the magnetic properties of $NdSb_xTe_{2-x+\delta}$ over the entire composition range. This work reveals an interesting nonmonotonic evolution of T_N accompanied by a systematic reorientation of moments from the in-plane to the out-of-plane direction with decreasing Sb content x . The rich magnetic phases in $NdSb_xTe_{2-x+\delta}$ provide useful insights for the evolution of magnetism in $LnSbTe$ materials, offering a good platform for tunable topological states.

ACKNOWLEDGMENTS

This work was primarily (synthesis and magnetic property up to 9 T) supported by the U.S. Department of Energy, Office of Science, Basic Energy Sciences program under Grant No. DE-SC0022006. M.M. and R.B. acknowledge μ -ATOMS, an Energy Frontier Research Center funded by DOE, Office of Science, Basic Energy Sciences, under Award DE-SC0023412 for part of the analysis. J.S. acknowledges the support from NIH under Award P20GM103429 for powder XRD. J. W. acknowledges the support from the U.S. National Science Foundation under Grant No. OSI-2328822 for structure refinement. J.H. acknowledges National Science Foundation under Grant No. DMR-1906383 for angular-dependent magnetization measurements using MPMS.

- [1] M. Z. Hasan and C. L. Kane, *Colloquium: Topological insulators*, *Rev. Mod. Phys.* **82**, 3045 (2010).
- [2] L. Fu, Topological crystalline insulators, *Phys. Rev. Lett.* **106**, 106802 (2011).
- [3] T. Liang, Q. Gibson, M. N. Ali, M. Liu, R. J. Cava, and N. P. Ong, Ultrahigh mobility and giant magnetoresistance in the Dirac semimetal Cd_3As_2 , *Nat. Mater.* **14**, 280 (2015).
- [4] Q. Li, D. E. Kharzeev, C. Zhang, Y. Huang, I. Pletikosić, A. V. Fedorov, R. D. Zhong, J. A. Schneeloch, G. D. Gu, and T. Valla, Chiral magnetic effect in $ZrTe_5$, *Nat. Phys.* **12**, 550 (2016).
- [5] Y.-S. Jho and K.-S. Kim, Interplay between interaction and chiral anomaly: Anisotropy in the electrical resistivity of interacting Weyl metals, *Phys. Rev. B* **87**, 205133 (2013).
- [6] S.-Y. Xu *et al.*, Observation of Fermi arc surface states in a topological metal, *Science* **347**, 294 (2015).
- [7] S.-Y. Xu *et al.*, Discovery of a Weyl fermion state with Fermi arcs in niobium arsenide, *Nat. Phys.* **11**, 748 (2015).
- [8] B. Q. Lv *et al.*, Experimental discovery of Weyl semimetal TaAs, *Phys. Rev. X* **5**, 031013 (2015).
- [9] S.-M. Huang *et al.*, A Weyl fermion semimetal with surface Fermi arcs in the transition metal monpnictide TaAs class, *Nat. Commun.* **6**, 7373 (2015).
- [10] A. Sakai *et al.*, Giant anomalous Nernst effect and quantum-critical scaling in a ferromagnetic semimetal, *Nat. Phys.* **14**, 1119 (2018).
- [11] S. N. Guin *et al.*, Anomalous Nernst effect beyond the magnetization scaling relation in the ferromagnetic Heusler compound Co_2MnGa , *NPG Asia Mater.* **11**, 16 (2019).
- [12] K. Manna *et al.*, From colossal to zero: Controlling the anomalous Hall effect in magnetic Heusler compounds via Berry curvature design, *Phys. Rev. X* **8**, 041045 (2018).
- [13] P. Li *et al.*, Giant room temperature anomalous Hall effect and tunable topology in a ferromagnetic topological semimetal Co_2MnAl , *Nat. Commun.* **11**, 3476 (2020).
- [14] E. Vilanova Vidal, G. Stryganyuk, H. Schneider, C. Felser, and G. Jakob, Exploring Co_2MnAl Heusler compound for anomalous Hall effect sensors, *Appl. Phys. Lett.* **99**, 132509 (2011).
- [15] E. Liu *et al.*, Giant anomalous Hall effect in a ferromagnetic kagome-lattice semimetal, *Nat. Phys.* **14**, 1125 (2018).

- [16] S. N. Guin *et al.*, Zero-field Nernst effect in a ferromagnetic kagome-lattice Weyl-semimetal $\text{Co}_3\text{Sn}_2\text{S}_2$, *Adv. Mater.* **31**, 1806622 (2019).
- [17] M. Kang *et al.*, Dirac fermions and flat bands in the ideal kagome metal FeSn , *Nat. Mater.* **19**, 163 (2020).
- [18] L. Ye *et al.*, Massive Dirac fermions in a ferromagnetic kagome metal, *Nature (London)* **555**, 638 (2018).
- [19] A. Sakai *et al.*, Iron-based binary ferromagnets for transverse thermoelectric conversion, *Nature (London)* **581**, 53 (2020).
- [20] K. Kim *et al.*, Large anomalous Hall current induced by topological nodal lines in a ferromagnetic van der Waals semimetal, *Nat. Mater.* **17**, 794 (2018).
- [21] S. Nakatsuji, N. Kiyohara, and T. Higo, Large anomalous Hall effect in a non-collinear antiferromagnet at room temperature, *Nature (London)* **527**, 212 (2015).
- [22] M. Ikhlas, T. Tomita, T. Koretsune, M.-T. Suzuki, D. Nishio-Hamane, R. Arita, Y. Otani, and S. Nakatsuji, Large anomalous Nernst effect at room temperature in a chiral antiferromagnet, *Nat. Phys.* **13**, 1085 (2017).
- [23] A. K. Nayak *et al.*, Large anomalous Hall effect driven by a nonvanishing Berry curvature in the noncollinear antiferromagnet Mn_3Ge , *Sci. Adv.* **2**, e1501870 (2016).
- [24] C. Wuttke *et al.*, Berry curvature unravelled by the anomalous Nernst effect in Mn_3Ge , *Phys. Rev. B* **100**, 085111 (2019).
- [25] T. Suzuki, R. Chisnell, A. Devarakonda, Y.-T. Liu, W. Feng, D. Xiao, J. W. Lynn, and J. G. Checkelsky, Large anomalous Hall effect in a half-Heusler antiferromagnet, *Nat. Phys.* **12**, 1119 (2016).
- [26] A. A. Burkov, Anomalous Hall effect in Weyl metals, *Phys. Rev. Lett.* **113**, 187202 (2014).
- [27] J. Noky, Y. Zhang, J. Gooth, C. Felser, and Y. Sun, Giant anomalous Hall and Nernst effect in magnetic cubic Heusler compounds, *npj Comput. Mater.* **6**, 77 (2020).
- [28] L. M. Schoop *et al.*, Tunable Weyl and Dirac states in the nonsymmorphic compound CeSbTe , *Sci. Adv.* **4**, eaar2317 (2018).
- [29] B. Lv, J. Chen, L. Qiao, J. Ma, X. Yang, M. Li, M. Wang, Q. Tao, and Z.-A. Xu, Magnetic and transport properties of low-carrier-density Kondo semimetal CeSbTe , *J. Phys.: Condens. Matter* **31**, 355601 (2019).
- [30] R. Singha, T. H. Salters, S. M. L. Teicher, S. Lei, J. F. Khoury, N. P. Ong, and L. M. Schoop, Evolving Devil's staircase magnetization from tunable charge density waves in nonsymmorphic Dirac semimetals, *Adv. Mater.* **33**, 2103476 (2021).
- [31] M. M. Hosen *et al.*, Discovery of topological nodal-line fermionic phase in a magnetic material GdSbTe , *Sci. Rep.* **8**, 13283 (2018).
- [32] R. Sankar *et al.*, Crystal growth and magnetic properties of topological nodal-line semimetal GdSbTe with antiferromagnetic spin ordering, *Inorg. Chem.* **58**, 11730 (2019).
- [33] S. Lei, A. Saltzman, and L. M. Schoop, Complex magnetic phases enriched by charge density waves in the topological semimetals $\text{GdSb}_x\text{Te}_{2-x-\delta}$, *Phys. Rev. B* **103**, 134418 (2021).
- [34] S. Lei, V. Duppel, J. M. Lippmann, J. Nuss, B. V. Lotsch, and L. M. Schoop, Charge density waves and magnetism in topological semimetal candidates $\text{GdSb}_x\text{Te}_{2-x-\delta}$, *Adv. Quantum Technol.* **2**, 1900045 (2019).
- [35] K. Pandey *et al.*, Magnetic topological semimetal phase with electronic correlation enhancement in SmSbTe , *Adv. Quantum Technol.* **4**, 2100063 (2021).
- [36] K. Pandey, R. Basnet, J. Wang, B. Da, and J. Hu, Evolution of electronic and magnetic properties in the topological semimetal $\text{SmSb}_x\text{Te}_{2-x}$, *Phys. Rev. B* **105**, 155139 (2022).
- [37] K. Pandey, R. Basnet, A. Wegner, G. Acharya, M. R. U. Nabi, J. Liu, J. Wang, Y. K. Takahashi, B. Da, and J. Hu, Electronic and magnetic properties of the topological semimetal candidate NdSbTe , *Phys. Rev. B* **101**, 235161 (2020).
- [38] R. Sankar, I. P. Muthuselvam, K. Rajagopal, K. Ramesh Babu, G. S. Murugan, K. S. Bayikadi, K. Moovendaran, C. Ting Wu, and G.-Y. Guo, Anisotropic magnetic properties of nonsymmorphic semimetallic single crystal NdSbTe , *Cryst. Growth Des.* **20**, 6585 (2020).
- [39] M. Yang, Y. Qian, D. Yan, Y. Li, Y. Song, Z. Wang, C. Yi, H. L. Feng, H. Weng, and Y. Shi, Magnetic and electronic properties of a topological nodal line semimetal candidate: HoSbTe , *Phys. Rev. Mater.* **4**, 094203 (2020).
- [40] S. Yue *et al.*, Topological electronic structure in the antiferromagnet HoSbTe , *Phys. Rev. B* **102**, 155109 (2020).
- [41] F. Gao, J. Huang, W. Ren, M. Li, H. Wang, T. Yang, B. Li, and Z. Zhang, Magnetic and transport properties of the topological compound DySbTe , *Phys. Rev. B* **105**, 214434 (2022).
- [42] F. Gao *et al.*, Magnetic and magnetotransport properties of the magnetic topological nodal-line semimetal TbSbTe , *Adv. Quantum Technol.* **6**, 2200163 (2023).
- [43] I. Plokhikh, V. Pomjakushin, D. J. Gawryluk, O. Zaharko, and E. Pomjakushina, Competing magnetic phases in LnSbTe ($\text{Ln} = \text{Ho}$ and Tb), *Inorg. Chem.* **61**, 11399 (2022).
- [44] I. Plokhikh, V. Pomjakushin, D. Jakub Gawryluk, O. Zaharko, and E. Pomjakushina, On the magnetic structures of 1:1:1 stoichiometric topological phases LnSbTe ($\text{Ln} = \text{Pr}$, Nd , Dy and Er), *J. Magn. Magn. Mater.* **583**, 171009 (2023).
- [45] Q. Xu, Z. Song, S. Nie, H. Weng, Z. Fang, and X. Dai, Two-dimensional oxide topological insulator with iron-pnictide superconductor LiFeAs structure, *Phys. Rev. B* **92**, 205310 (2015).
- [46] L. M. Schoop, M. N. Ali, C. Straßer, A. Topp, A. Varykhalov, D. Marchenko, V. Duppel, S. S. P. Parkin, B. V. Lotsch, and C. R. Ast, Dirac cone protected by non-symmorphic symmetry and three-dimensional Dirac line node in ZrSiS , *Nat. Commun.* **7**, 11696 (2016).
- [47] J. Hu *et al.*, Evidence of topological nodal-line fermions in ZrSiSe and ZrSiTe , *Phys. Rev. Lett.* **117**, 016602 (2016).
- [48] R. Lou, J. Z. Ma, Q. N. Xu, B. B. Fu, L. Y. Kong, Y. G. Shi, P. Richard, H. M. Weng, Z. Fang, S. S. Sun, Q. Wang, H. C. Lei, T. Qian, H. Ding, and S. C. Wang, Emergence of topological bands on the surface of ZrSnTe crystal, *Phys. Rev. B* **93**, 241104(R) (2016).
- [49] M. Neupane *et al.*, Observation of topological nodal fermion semimetal phase in ZrSiS , *Phys. Rev. B* **93**, 201104(R) (2016).
- [50] D. Takane, Z. Wang, S. Souma, K. Nakayama, C. X. Trang, T. Sato, T. Takahashi, and Y. Ando, Dirac-node arc in the topological line-node semimetal HfSiS , *Phys. Rev. B* **94**, 121108(R) (2016).
- [51] M. M. Hosen *et al.*, Tunability of the topological nodal-line semimetal phase in ZrSiX -type materials ($X = \text{S}$, Se , Te), *Phys. Rev. B* **95**, 161101(R) (2017).
- [52] C. Chen, X. Xu, J. Jiang, S.-C. Wu, Y. P. Qi, L. X. Yang, M. X. Wang, Y. Sun, N. B. M. Schröter, H. F. Yang *et al.*, Dirac line nodes and effect of spin-orbit coupling in the

- nonsymmorphic critical semimetals $MSiS$ ($M = \text{Hf, Zr}$), *Phys. Rev. B* **95**, 125126 (2017).
- [53] B.-B. Fu *et al.*, Dirac nodal surfaces and nodal lines in ZrSiS , *Sci. Adv.* **5**, eaau6459 (2019).
- [54] A. Topp, J. M. Lippmann, A. Varykhalov, V. Duppel, B. V. Lotsch, C. R. Ast, and L. M. Schoop, Non-symmorphic band degeneracy at the Fermi level in ZrSiTe , *New J. Phys.* **18**, 125014 (2016).
- [55] S. Pezzini, M. R. van Delft, L. M. Schoop, B. V. Lotsch, A. Carrington, M. I. Katsnelson, N. E. Hussey, and S. Wiedmann, Unconventional mass enhancement around the Dirac nodal loop in ZrSiS , *Nat. Phys.* **14**, 178 (2018).
- [56] Y. Shao *et al.*, Electronic correlations in nodal-line semimetals, *Nat. Phys.* **16**, 636 (2020).
- [57] S. Regmi, R. Smith, A. P. Sakhya, M. Sprague, M. I. Mondal, I. B. Elius, N. Valadez, A. Ptok, D. Kaczorowski, and M. Neupane, Observation of gapless nodal-line states in NdSbTe , *Phys. Rev. Mater.* **7**, 044202 (2023).
- [58] S. Regmi, G. Dhakal, F. C. Kabeer, N. Harrison, F. Kabir, A. P. Sakhya, K. Gofryk, D. Kaczorowski, P. M. Oppeneer, and M. Neupane, Observation of multiple nodal lines in SmSbTe , *Phys. Rev. Mater.* **6**, L031201 (2022).
- [59] K. Pandey, L. Sayler, R. Basnet, J. Sakon, F. Wang, and J. Hu, Crystal growth and electronic properties of LaSbSe , *Crystals* **12**, 1663 (2022).
- [60] S. Acharya, K. Pandey, R. Basnet, G. Acharya, M. R. U. Nabi, J. Wang, and J. Hu, Single crystal growth and characterization of topological semimetal ZrSnTe , *J. Alloys Compd.* **968**, 171903 (2023).
- [61] S. Lei *et al.*, Band engineering of Dirac semimetals using charge density waves, *Adv. Mater.* **33**, 2101591 (2021).
- [62] P. Li *et al.*, Charge density wave and weak Kondo effect in a Dirac semimetal CeSbTe , *Sci. China: Phys., Mech. Astron.* **64**, 237412 (2021).
- [63] T. H. Salters, F. Orlandi, T. Berry, J. F. Khoury, E. Whittaker, P. Manuel, and L. M. Schoop, Charge density wave-templated spin cycloid in topological semimetal $\text{NdSb}_x\text{Te}_{2-x-\delta}$, *Phys. Rev. Mater.* **7**, 044203 (2023).
- [64] S. Klemenz, S. Lei, and L. M. Schoop, Topological semimetals in square-net materials, *Annu. Rev. Mater. Res.* **49**, 185 (2019).
- [65] J. Hu, Y. Zhu, X. Gui, D. Graf, Z. Tang, W. Xie, and Z. Mao, Quantum oscillation evidence for a topological semimetal phase in ZrSnTe , *Phys. Rev. B* **97**, 155101 (2018).
- [66] K. Stöwe, Crystal structure, magnetic properties and band gap measurements of NdTe_{2-x} ($x = 0.11(1)$), *Z. Kristallogr. - Cryst. Mater.* **216**, 215 (2001).
- [67] H. Poddig, P. Gebauer, K. Finzel, K. Stöwe, and T. Doert, Structural variations and bonding analysis of the rare-earth metal tellurides $RETe_{1.875\pm\delta}$ ($RE = \text{Ce, Pr, Sm, Gd}$; $0.004 \leq \delta \leq 0.025$), *Inorg. Chem.* **60**, 11231 (2021).
- [68] C. J. Müller, U. Schwarz, and T. Doert, High-pressure syntheses of lanthanide polysulfides and polyselenides $LnX_{1.9}$ ($Ln = \text{Gd-Tm}$, $X = \text{S, Se}$), *Z. Anorg. Allg. Chem.* **638**, 2477 (2012).
- [69] S.-M. Park, S.-J. Park, and S.-J. Kim, The superstructure of semiconducting SmTe_{2-x} , *J. Solid State Chem.* **140**, 300 (1998).
- [70] H. Poddig, T. Donath, P. Gebauer, K. Finzel, M. Kohout, Y. Wu, P. Schmidt, and T. Doert, Rare earth metal polytellurides $RETe_{1.8}$ ($RE = \text{Gd, Tb, Dy}$) – Directed synthesis, crystal and electronic structures, and bonding features, *Z. Anorg. Allg. Chem.* **644**, 1886 (2018).
- [71] R. Wang, H. Steinfink, and W. F. Bradley, The crystal structure of lanthanum telluride and of tellurium-deficient neodymium telluride, *Inorg. Chem.* **5**, 142 (1966).
- [72] K. Stöwe, Crystal structure and magnetic properties of CeTe_2 , *J. Alloys Compd.* **307**, 101 (2000).
- [73] K. Stöwe, Die kristallstruktur von PrTe_2 , *Z. Anorg. Allg. Chem.* **626**, 803 (2000).
- [74] K. Stöwe, Crystal structure and electronic band structure of LaTe_2 , *J. Solid State Chem.* **149**, 155 (2000).
- [75] E. Lee, D. H. Kim, J. D. Denlinger, J. Kim, K. Kim, B. I. Min, B. H. Min, Y. S. Kwon, and J.-S. Kang, Angle-resolved and resonant photoemission spectroscopy study of the Fermi surface reconstruction in the charge density wave systems CeTe_2 and PrTe_2 , *Phys. Rev. B* **91**, 125137 (2015).
- [76] J.-S. Kang *et al.*, Fermi surface reconstruction in CeTe_2 induced by charge density waves investigated via angle resolved photoemission, *Phys. Rev. B* **85**, 085104 (2012).
- [77] K. Y. Shin, V. Brouet, N. Ru, Z. X. Shen, and I. R. Fisher, Electronic structure and charge-density wave formation in $\text{LaTe}_{1.95}$ and $\text{CeTe}_{2.00}$, *Phys. Rev. B* **72**, 085132 (2005).
- [78] D. R. Garcia, G.-H. Gweon, S. Y. Zhou, J. Graf, C. M. Jozwiak, M. H. Jung, Y. S. Kwon, and A. Lanzara, Revealing charge density wave formation in the LaTe_2 system by angle resolved photoemission spectroscopy, *Phys. Rev. Lett.* **98**, 166403 (2007).
- [79] Y. S. Shin, C. W. Han, B. H. Min, H. J. Lee, C. H. Choi, Y. S. Kim, D. L. Kim, and Y. S. Kwon, Anisotropic magnetization in RTe_2 ($R: \text{Ce, Pr, Gd and Sm}$), *Phys. B (Amsterdam, Neth.)* **291**, 225 (2000).
- [80] R. J. Birgeneau, Magnetic moment reduction via the orbit-lattice interaction for Ce^{3+} in rare-earth ethyl sulfates, *Phys. Rev. Lett.* **19**, 160 (1967).
- [81] T. Tsuchida, A. Hashimoto, and Y. Nakamura, Crystal field effect on the magnetic properties of $\text{Ce}_x\text{La}_{1-x}\text{Bi}$, *J. Phys. Soc. Jpn.* **36**, 685 (1974).
- [82] A. Galler, S. Ener, F. Maccari, I. Dirba, K. P. Skokov, O. Gutfleisch, S. Biermann, and L. V. Pourovskii, Intrinsically weak magnetic anisotropy of cerium in potential hard-magnetic intermetallics, *npj Quantum Mater.* **6**, 1 (2021).
- [83] L. L. Hirst, Theory of the coupling between conduction electrons and moments of 3d and 4f ions in metals, *Adv. Phys.* **27**, 231 (1978).
- [84] L. Pourovskii, V. Vildosola, S. Biermann, and A. Georges, Local moment vs. Kondo behavior of the 4f-electrons in rare-earth iron oxypnictides, *Europhys. Lett.* **84**, 37006 (2008).
- [85] M. Nicklas, S. Kirchner, R. Borth, R. Gumenuk, W. Schnelle, H. Rosner, H. Borrmann, A. Leithe-Jasper, Yu. Grin, and F. Steglich, Charge-doping-driven evolution of magnetism and non-Fermi-liquid behavior in the filled skutterudite $\text{CePt}_4\text{Ge}_{12-x}\text{Sb}_x$, *Phys. Rev. Lett.* **109**, 236405 (2012).
- [86] R. Skomski and D. J. Sellmyer, Anisotropy of rare-earth magnets, *J. Rare Earths* **27**, 675 (2009).
- [87] E. Sarantopoulou, S. Kobe, Z. Kollia, B. Podmiljšak, P. J. McGuinness, G. Dražić, and A. C. Cefalas, Magnetic and optical properties of single $4f^n$ and mixed $4f^{n-1} 5d$ electronic configurations of trivalent rare earth ions in wide band gap dielectric crystals, *J. Magn. Magn. Mater.* **267**, 182 (2003).

- [88] J.-R. Soh, S. M. Tobin, H. Su, I. Zivkovic, B. Ouladdiaf, A. Stunault, J. A. Rodríguez-Velamazán, K. Beauvois, Y. Guo, and A. T. Boothroyd, Magnetic structure of the topological semimetal YbMnSb₂, *Phys. Rev. B* **104**, L161103 (2021).
- [89] R. G. Moore *et al.*, Topological electronic structure evolution with symmetry-breaking spin reorientation in Fe_{1-x}Co_xSn, *Phys. Rev. B* **106**, 115141 (2022).
- [90] Z. Lin *et al.*, Dirac fermions in antiferromagnetic FeSn kagome lattices with combined space inversion and time-reversal symmetry, *Phys. Rev. B* **102**, 155103 (2020).
- [91] S. H. Lee *et al.*, Evidence for a magnetic-field-induced ideal type-II Weyl state in antiferromagnetic topological insulator Mn(Bi_{1-x}Sb_x)₂Te₄, *Phys. Rev. X* **11**, 031032 (2021).